ALMA MATER STUDIORUM
UNIVERSITÀ DI BOLOGNA

ARCHIVIO ISTITUZIONALE
DELLA RICERCA

Alma Mater Studiorum Università di Bologna
Archivio istituzionale della ricerca

State of stress and stress rotations: Quantifying the role of surface topography and subsurface density contrasts in magmatic rift zones (Eastern Rift, Africa)

This is the final peer-reviewed author's accepted manuscript (postprint) of the following publication:

Published Version:
Oliva, S.J., Ebinger, C.J., Rivalta, E., Williams, C.A., Wauthier, C., Currie, C.A. (2022). State of stress and stress rotations: Quantifying the role of surface topography and subsurface density contrasts in magmatic rift zones (Eastern Rift, Africa). EARTH AND PLANETARY SCIENCE LETTERS, 584, 1-9 [10.1016/j.epsl.2022.117478].

Availability:
This version is available at: https://hdl.handle.net/11585/883903 since: 2022-05-03

Published:
DOI: http://doi.org/10.1016/j.epsl.2022.117478

Terms of use:

Some rights reserved. The terms and conditions for the reuse of this version of the manuscript are specified in the publishing policy. For all terms of use and more information see the publisher's website.

This item was downloaded from IRIS Università di Bologna (https://cris.unibo.it/).
When citing, please refer to the published version.

(Article begins on next page)

12 October 2024

This is the final peer-reviewed accepted manuscript of:

Sarah Jaye Oliva, Cynthia J. Ebinger, Eleonora Rivalta, Charles A. Williams, Christelle Wauthier, Claire A. Currie, *State of stress and stress rotations: Quantifying the role of surface topography and subsurface density contrasts in magmatic rift zones (Eastern Rift, Africa)*, Earth and Planetary Science Letters, Volume 584, 2022, 117478.

The final published version is available online at: https://doi.org/10.1016/j.epsl.2022.117478

Rights / License:

The terms and conditions for the reuse of this version of the manuscript are specified in the publishing policy. For all terms of use and more information see the publisher's website.

This item was downloaded from IRIS Università di Bologna (https://cris.unibo.it/)

When citing, please refer to the published version.

Highlights

State of stress and stress rotations: Quantifying the role of surface topography and subsurface density contrasts in magmatic rift zones (Eastern Rift, Africa)

S. J. Oliva, C. J. Ebinger, E. Rivalta, C. A. Williams, C. Wauthier, C. Currie

- Surface topography influences shallow stress localization
- Subsurface density contrasts influences lower crustal stress localization
- Topography, subsurface, and extension can produce local stress rotation
- Subsurface stresses are important in complete spatial understanding of rift tectonics

State of stress and stress rotations: Quantifying the role of surface topography and subsurface density contrasts in magmatic rift zones (Eastern Rift, Africa)

S. J. Oliva[a,b,c,], C. J. Ebinger[a], E. Rivalta[d,e], C. A. Williams[f], C. Wauthier[g], C. Currie[h]

[a] *Tulane University, New Orleans, LA, USA*
[b] *University of British Columbia, Vancouver, BC, Canada*
[c] *University of Victoria, Victoria, BC, Canada*
[d] *GFZ Helmholtz Centre Potsdam German Research Centre for Geosciences, Potsdam, Germany*
[e] *Alma Mater Studiorum Università di Bologna, Bologna, Italy*
[f] *GNS Science, Lower Hutt, New Zealand*
[g] *Pennsylvania State University, State College, PA, USA*
[h] *University of Alberta, Edmonton, AB, Canada*

Abstract

In rift settings, the crustal stress field is dominated by extension, which leads to rift-parallel topography and basin alignments. However in some continental rift systems, some observables of the orientation of principal stresses show substantial deviations from these patterns. Such stress field rotations are currently poorly understood and could reflect the critical role of rift magmatism in the creation of topography, the plate state-of-stress, and volcanic and tectonic processes. Yet the role of magma intrusions, crustal thinning, and rift basin and flank topography on rift zone stress field rotations remain poorly quantified. The seismically- and volcanically-active Magadi-Natron-Manyara region of the East African Rift shows a 60° local stress field rotation with re-

Email address: soliva@uvic.ca (S. J. Oliva)

spect to regional extension. Here, we test the hypothesis that such rotation is due to the cumulative effects of surface and subsurface loads (lateral subsurface density contrasts). We use analytical and calibrated numerical models of magmatic rift zones to simulate lithospheric deformation in the presence of magma bodies, crustal thinning, and topography to quantify their effect on intrusions and fault kinematics in a rift setting. Our 3D static models of a weakly extended rift suggest that surface topography influences shallow stress localization, whereas subsurface density contrasts play a larger role in lower crustal stress localization. Both patterns suggest a preferred region for melt storage beneath the rift valley. We show that the interaction between topography, crustal thinning, extension, and a pressurized magma reservoir could generate principal stress orientations consistent with the local stress rotation observed from earthquake focal mechanisms. Our results demonstrate how rift topography and the geometry of crustal thinning can guide magmatism and strain localization, highlighting the need for a three-dimensional treatment of rift kinematics.
Keywords: rift, continental rifting, tectonics, stress, topography

---

1. Introduction

Continental rift zones are sites of intraplate stretching, commonly with adiabatic decompression melting accompanying lithospheric thinning. Large fault systems bound the rift and are segmented along the length of the rift, with strain linkage by rift-oblique transfer faults and relay ramps (e.g., Acocella et al., 2005; Ebinger, 1989; Larsen, 1988; Tibaldi et al., 2020). Volcanoes and underlying crustal magma chambers cause fundamental changes

to the density and thermal structure, load the plates, and change the state of stress within the crust and mantle lithosphere (e.g., Karlstrom et al., 2009). In magmatic regions, the local stress field induced by volcanic edifice loading/unloading (e.g., Kervyn et al., 2009; Maccaferri et al., 2014) and/or weak zones (e.g., Corti et al., 2004) then influence subsequent magma migration and vent distribution (e.g., Karlstrom et al., 2009; Rivalta et al., 2019) Generally, dike and fracture orientations are favored perpendicular to the direction of the least compressive stress (e.g., Pollard, 1987; Sibson, 1985). Although published two-dimensional models of loading on plates without in-plane regional stresses offer insight (e.g., Karlstrom et al., 2009), a critical gap in understanding remains on how surface (e.g., volcanoes, rift flanks) and subsurface intrusions (sills, dikes, magma chambers) combine with regional stresses in rift zones. In this study, we aim to address this gap and complement existing conceptual models of magmatic rift zone structural patterns (e.g., Magee et al., 2016; Muirhead et al., 2015; Tibaldi et al., 2020).

We build analytical and numerical models of magmatic rift zones to simulate lithospheric deformation in the presence of magma bodies to quantify the interactions between surface and subsurface loading on intrusions and fault kinematics in a rift setting. We use the open-source finite element modeling package PyLith v2.2.1 (Aagaard et al., 2013, 2017a,b) to build two- (2D) and three-dimensional (3D) physics-based static models, calibrated to analytical stress models, to quantify the effects of loading on the crustal state of stress. We probe how inclusions (subsurface volumes of density different than host material, e.g., magmatic intrusions) and loads/excavations of different spatial scales guide local stress field rotation and strain localization to favor the

initiation of extensional faults, dikes, and eruptive centers oriented obliquely to the regional extension direction (e.g., Ebinger, 1989; Acocella et al., 2005). Our approach is two-fold: we first evaluate model sensitivities to topography and subsurface density contrasts separately, and then we compare our models with observed stress indicators (i.e., earthquake locations and focal mechanisms). The static elastic modeling approach allows us to consider each load separately, and summatively.

2. Tectonic Background

The Magadi-Natron-Manyara basins are located in the southernmost sector of the magmatic Eastern rift (Fig. 1). The Natron basin, which contains lavas and sedimentary strata dating to ∼3 Ma, developed in metasomatized Archaean lithosphere, as confirmed by mantle xenoliths (Mana et al., 2015; Aulbach et al., 2011; McHenry et al., 2011; Foster et al., 1997). The present-day Natron basin is a N-S trending half-graben bounded by a monocline to the east, that formed during a major phase of faulting at ∼1.2–1 Ma when the east-dipping Songo border fault developed within the original wider basin (Foster et al., 1997; Muirhead et al., 2016). Gelai volcano formed at ∼1 Ma whereas carbonatite volcano Oldoinyo Lengai (∼0.37 Ma, OL, Fig. 1) post-dates the main phases of rift faulting and basaltic volcanism (Mana et al., 2015; Foster et al., 1997; Muirhead et al., 2015, 2016). The Naibor Soito monogenetic cone field (NS, Fig. 1) lies between Oldoinyo Lengai and Gelai (e.g., Weinstein et al., 2017; Dawson, 1992).

The region is an ideal place to quantify the different loading contributions on crustal state-of-stress because the 2013-2014 Continental Rift and Fluid-

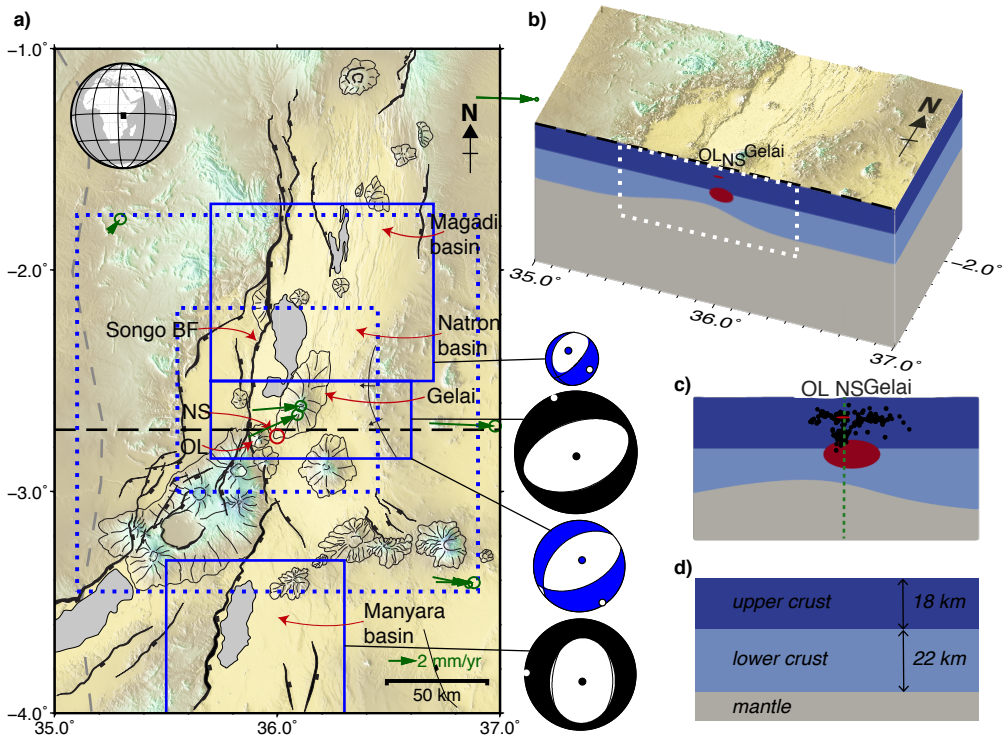

Figure 1: Study area and model geometry. a) Map of the Magadi-Natron-Manyara basins of the East African Rift system. Inset shows the location on the globe. Solid blue boxes enclose areas of seismicity analyzed by Weinstein et al. (2017) and the corresponding summed moment tensors (blue beachballs are from local focal mechanisms, black beachballs are from teleseismic focal mechanisms) that reveal along-axis local stress rotation. Green arrows are GNSS velocity vectors for a Nubia-fixed model with their error ellipses (King et al., 2019). Large dotted blue box describes the extent of the 3D model domain, with higher resolution topography (1 km) within the smaller dotted box (nodal spacing doubles at every step outward until the edge of the domain). The black dashed line represents the E-W transect at 2.72°S latitude which is used in the 2D models. Faults and edifices are from Muirhead et al. (2015). BF: border fault; NS: Naibor Soito; OL: Oldoinyo Lengai. b) Perspective figure looking northwest shows a section of the 3D model domain sliced along 2.72°S. The upper crust is dark blue, lower crust is light blue, mantle is gray, and the sill and magma chamber are red. c) Double-difference earthquake locations within 5 km north and south of the cross-section (dotted white box in b). Dashed green line ($x = 2750$ m, where $x = 0$ is 36° longitude) indicates the location of the 1D profile in Fig. 3. d) Reference model thicknesses.

Tectonic Interaction (CRAFTI) network (Weinstein et al., 2017), as well as the recent Seismic and Infrasound Networks to study the volcano Oldoinyo Lengai (SEISVOL) project in 2019-2020 (Reiss et al., 2021), provide excellent constraints for modeling. Nubia-fixed rigid plate models predict 2–5 mm/yr approximately E-W opening in the area (Saria et al., 2014; King et al., 2019) (green arrows, Fig. 1). Receiver function studies show crustal thinning from 40 km to 29 km in the middle of the rift valley (Plasman et al., 2017). A velocity contrast at ∼18 km depth is interpreted from a clear negative peak in receiver functions around 3 s, which is also evident in the tomography (Plasman et al., 2017; Roecker et al., 2017). Seismicity and tomography studies (from the regional CRAFTI network) image a magma chamber and sill complex in the subsurface (Weinstein et al., 2017; Roecker et al., 2017; Reiss et al., 2021). The local SEISVOL network allowed further detailed seismic studies and identified clusters beneath the Naibor Soito volcanic field at 5–10 km depth interpreted as stress concentrations at the edges of pressurized sills, and at 12–18 km depth representing the top of the lower-crustal magma chamber, confirming that some seismicity patterns observed in the earlier network are consistent over longer timescales (Reiss et al., 2021). Focal mechanisms of both local and teleseismic earthquakes reveal an along-axis local stress rotation of ∼60° in the OL-NS-Gelai complex (∼N150°E extension), relative to the ∼E-W regional extension indicated by seismic and geodetic data (Weinstein et al., 2017) (Fig. 1). Reiss et al. (2021) report a mean T-axis direction of NW-SE in the OL-NS-Gelai area, noting that beneath Naibor Soito, there was no dominant mechanism above the magma chamber (below 13 km) and in the sill complex (5–7 km; 9–11

km). Instead, the local stress rotation (∼N-S T-axes) was mainly observed at ∼7–9 km depth. A detailed study of the variations in fault, dike, and cone orientations in the East African Rift suggest that in different regions, different stresses dominate: the regional stress state, magma overpressure and volcanic edifice load, pre-existing structures, or local stress rotations due to mechanical interactions of rift basin segments (Muirhead et al., 2015). A separate study of East African Rift volcanoes hypothesized that rift-oblique dikes and fissures were either due to lithospheric heterogeneities or magmatic processes (Wadge et al., 2016). Since dikes are subvertical (e.g., Calais et al., 2008; Muirhead et al., 2015; Weinstein et al., 2017), it is unlikely that they reactivated Archaean and Pan-African strain fabrics that dip at angles $\leq 45°$ (e.g., Le Gall et al., 2008; Smith and Mosley, 1993), although the pre-existing oblique fabric might influence later structures by lowering the residual strength of the rock.

In June–August 2007, the Naibor Soito complex and the flanks of Gelai were the site of 50+ $3.6 < m_b < 5.9$ earthquakes and diking with associated opening of 1.0–2.4 m, followed by eruption at Oldoinyo Lengai through 2008 (Baer et al., 2008; Biggs et al., 2009; Calais et al., 2008). During the seismomagmatic sequence, 65% of the total geodetic moment release was attributed to dike opening, highlighting the importance of magma intrusions in accommodating rift opening (Calais et al., 2008). New geophysical results reinterpret the 2007 diking event to have occurred above a shallow sill complex underlain by a low-velocity mid-crustal magma mush (Oliva et al., 2019; Roecker et al., 2017; Weinstein et al., 2017).

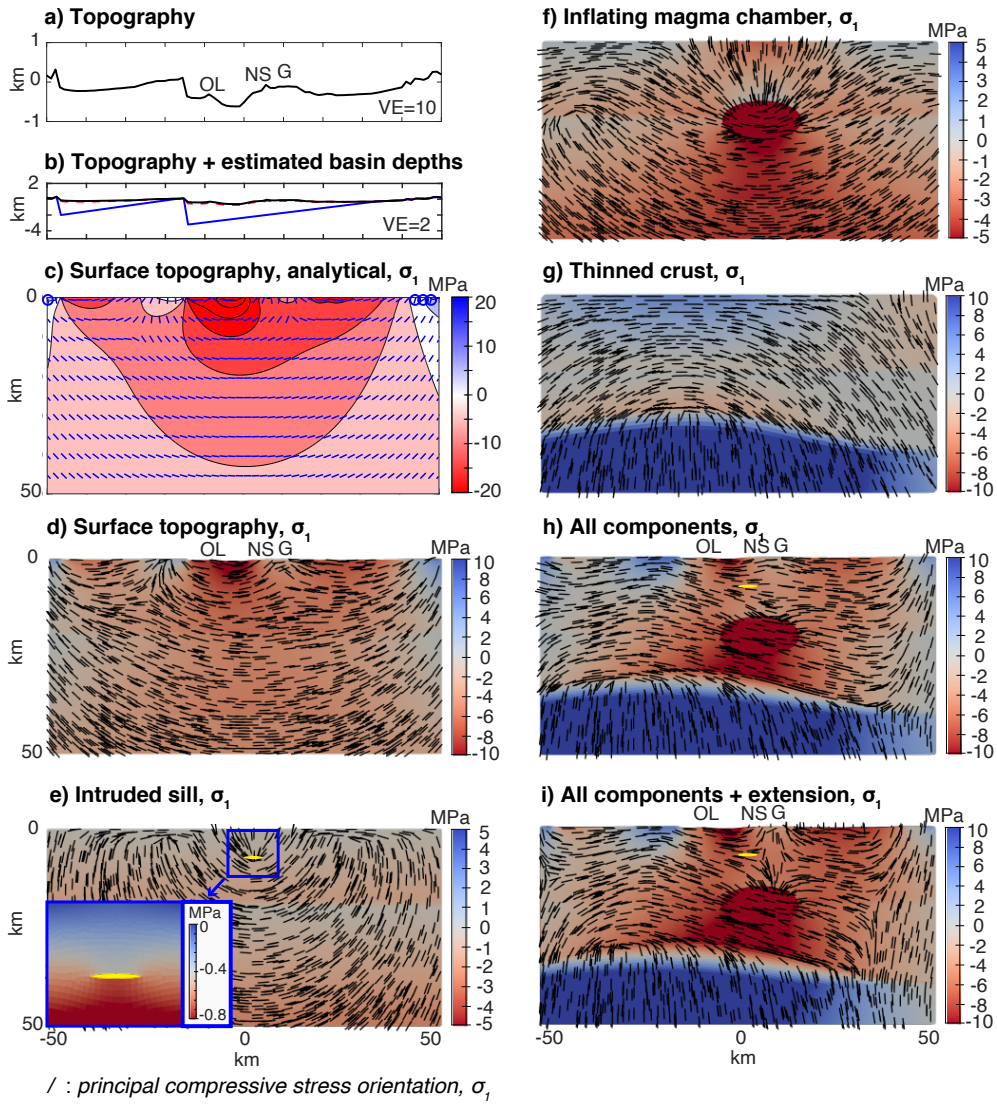

Figure 2: Two-dimensional static model results. Cross-sections are E-W transects at 2.72°S, centered at 36°E (black dashed line in Fig. 1). a) Topography with 10× vertical exaggeration. b) Topography (black), estimated basin depths (blue) (Birt et al., 1997), and topography corrected for low-density basin fill (red dashed) with 2× vertical exaggeration. c) Analytical model of topographic loading (as in b) colored by stress magnitude (positive stress values are compressive). Line segments (blue on c and black elsewhere) are orientations of the principal stress (greatest compressive), σ_1. d–i) Numerical models of separate stress contributions of each rift component colored by stress magnitude. Stresses are deviations in gravitational stress ($g = 9.78$ m/s^2) with respect to a reference model: a uniform-thickness three-layer model with no magmatic systems. Numerical models show the separate effects of d) surface topography, e) an intruded sill (density contrast, yellow ellipse), f) an overpressurized magma chamber (density contrast and outward pressure), g) the Moho topography of a thinned crust, h) the combined effects of the four above-mentioned components, and i) the combined effects of all components including a displacement boundary condition to represent regional extension. OL: Oldoinyo Lengai, NS: Naibor Soito, G: Gelai.

3. Modeling approach and limitations

The crustal stress field is determined by the combination of stress-generating mechanisms (e.g., topographic loads, magma overpressure) and stress-relieving mechanisms (e.g., inelastic deformation, earthquakes). Here we focus on the former and treat the location and orientation of dikes and faults, as well as Global Navigation Satellite System (GNSS)-derived plate motion directions, as stress indicators. Crustal stresses control the predominant orientation of faults and the slip direction during earthquakes. Elastic stresses cycle phases of stress accumulation from the action of tectonic forces, punctuated by release events during major earthquakes. Constraining the pattern of elastic stresses at the regional, "tectonic environment" scale can help us understand these cycles and any stress rotation occurring.

To investigate first-order stress contributions of different components, we use present-day constraints for model geometry and evaluate static elastic stress models. With elastic models, we take advantage of linear superposition, wherein the net response to various components is the sum of the individual responses. This enables us to investigate each component of interest separately, while also being able to superimpose them to see the combined effect. Note that because time is an important aspect of ductile behavior, our static models cannot capture time-dependent rheological behavior.

In our models, we do not include faults as discontinuities and instead only consider the influence of surface topography, magma bodies, and crustal thinning to the stresses on a continuous crustal model. Faults both respond to and influence stress orientations, and modeling this feedback is difficult to capture in a static model and would be more appropriately done in a separate

dynamic modeling study. In addition, long-wavelength gravitational loads (such as those considered in this study) would dominate the short-wavelength effect of faults, except the largest faults (e.g., Maccaferri et al., 2014).

The abovementioned modeling decisions enable us to evaluate the state-of-stress within the continental crust, specifically the stress contributions of topography, crustal thinning, and magma bodies. Our goal is to quantify the resulting spatial stress patterns, to summarize first-order effects, and discuss the implications of our findings on the evolution of magmatic and fault systems. Our goal is not to simulate the detailed state-of-stress within the Natron-Magadi system. Hence, we avoid additional model complexities to ensure that the first-order effects we are interested in are not obscured. While viscous stresses are certainly important in the long-term evolution of the system, in the short timescales of earthquakes and dikes, the elastic component of the stresses are more important. The caveat is that our results are generally limited to the strong part (∼upper crust) of the lithosphere, where viscous effects are less important.

4. Methods

4.1. Model geometry

Our 2D models are about 200 km across and 100 km deep, and the 3D models are about 200 km × 200 km × 100 km (Fig. 1c,d). We only interpret the results within a smaller 100 km (× 100 km) × 50 km box embedded within the larger domain to avoid effects due to boundary conditions (see dashed white box on Fig. 1b). The model geometry was built from the Shuttle Radar Topography Mission (SRTM) 90m digital elevation database

Layer	Depths (km)	ρ (kg/m^3)	Vs (km/s)	Vp (km/s)	λ ($\times 10^{10}$)	μ ($\times 10^{10}$)
upper crust	0–18	2761	3.6	6.2	3.46	3.58
lower crust	18–22	2833	3.4	6.5	5.38	3.29
mantle	22–100	3300	4.5	8.1	8.29	6.68
sill	$\sim$7	2661	3.6	6.2	3.33	3.45
chamber	15–25	2661	3.3	5.5	2.25	2.90

Table 1: Material properties. First-order crustal densities (ρ) were estimated from seismic velocities (Vp, Vs) (Plasman et al., 2017; Roecker et al., 2017; Tiberi et al., 2018), using an empirical relation between crustal density and seismic velocity (Brocher, 2005). The mantle velocity and density were adapted from the velocity models of Plasman et al. (2017) and Tiberi et al. (2018). Sill and magma chamber velocities are taken from Roecker et al. (2017). Lamé parameters are calculated from density and seismic velocities: $\mu = \rho Vs^2$; $\lambda = \rho Vp^2 - 2\mu$.

v.4 (Jarvis et al., 2008), estimated basin depths from refraction and wide-angle reflection data (Birt et al., 1997), and crustal tomography (Roecker et al., 2017). The Moho structure was constrained from receiver functions (Plasman et al., 2017) assuming a velocity contrast at 18 km (Plasman et al., 2017; Roecker et al., 2017) and that unstretched crust is 40 km thick (Mansur et al., 2014; Tugume et al., 2012).

4.2. Analytical models

We first modeled topography and extension using analytical 2D models. Because our study area sits at the edge of the uplifted Tanzanian craton and we do not include dynamic topography in the models, we removed a long-wavelength trend from the SRTM topography. Detrended topography with

adjustments based on lower density basin fill (dotted red line, Fig. 2b) was modeled analytically as a line load in an elastic 2D half-space (e.g., Dahm, 2000). Basin-fill adjustments were made such that the surface load of the adjusted topography with uniform density ($\rho = 2.7$ g/cm^2) is equivalent to that of original topography with lower-density basins ($\rho = 2.55$ g/cm^2, Birt et al. (1997)).

4.3. Numerical models

The 2D and 3D finite-element (FE) models were built using the meshing software Trelis and modeled with regional extension and gravity using the open-source lithospheric modeling package PyLith (Aagaard et al., 2013, 2017a,b). PyLith was specifically designed for the solution of tectonic problems, and is capable of solving static, quasi-static, and dynamic problems in geophysics. We do not consider time and thermomechanical effects in our modeling efforts, and we therefore restrict our models to static elastic simulations without faults. Sample Trelis and PyLith input files are provided in Supplementary materials SM3–SM4.

4.3.1. Mesh generation

In 2D models, we mesh with quadrilateral elements (paving) with a mesh size of 0.5 km within the crust and the magma chamber, 0.2 km within the sill, and 0.8 km in the mantle. In 3D models, we mesh with tetrahedral elements and implement adaptive meshing to create a mesh with finer spacing along areas of interest that gets coarser towards the lateral and bottom boundaries. We use Trelis' bias sizing function to produce gradients of mesh size that respect the predefined discretization size along curves (see Supplementary

material SM2). The discretization size is set to 1 km along the surface topography, 1 km along the magma chamber boundary, 0.2 km along the sill boundary, 2.5 km along the interface at 18 km depth, 5 km along the Moho, and 10 km at the bottom of the model.

4.3.2. Material parameters

Using an empirical relation between crustal density and seismic velocity (Brocher, 2005), the first-order crustal densities were estimated from seismic velocities (Plasman et al., 2017; Roecker et al., 2017; Tiberi et al., 2018). The mantle velocity and density were adapted from the velocity models of Plasman et al. (2017) and Tiberi et al. (2018). In the cases with the sill and the magma chamber, magma density was taken to be slightly lower than surrounding rock with seismic velocities taken from Roecker et al. (2017), which imposes a buoyancy effect on the models. Although temperature, pressure, composition, and hydration state also influence density, seismic velocity, and rheology (e.g., Guerri et al., 2015), these are not considered in this study; that is, the elastic parameters (Lamé constants) used in the numerical model were calculated using density and seismic velocities only (Table 1). Because the static models do not include the time component, ductile behavior is not captured (e.g., Maccaferri et al., 2014).

4.3.3. Initial and boundary conditions

We first evaluated separate stress contributions of each rift structure, then later combined them all together. Stress contributions were calculated as deviations in gravitational stress (with acceleration due to gravity $g = 9.78$ m/s^2) with respect to the assumed lithostatic equilibrium state of a reference

model (Fig. 1d, see Supplementary material Fig. SM1): a uniform-thickness three-layer model with no magmatic systems and no topographic variations ($z = 0$ on Fig. 2a). Topography and crustal thinning were represented by modifications to the model geometry. The upper-crustal sill was modeled as an ellipsoid 500 m thick, circular in plan-view (major axis of 5 km), centered at 7 km depth. The mid-crustal magma chamber, which likely consists of geometrically complex zones of mush and melt (Cashman et al., 2017), was modeled as a 10 km thick, 20 km wide spheroidal inclusion, centered at 20 km depth, with an outward-directed pressure boundary condition of 10 MPa to represent inflation (Allmann and Shearer, 2009).

For all models, a roller boundary condition was imposed on the bottom of the block and a free surface on the top. For models without extension, the lateral boundaries had a zero-displacement boundary condition. For extensional models, five meters of displacement was imposed on each lateral side, 2.5×10^{-5} of strain, which corresponds to $\sim$3 MPa horizontal upper crustal stress. The choice of imposed stresses is guided by the assumption that deviatoric stresses significantly larger than 10 MPa would be released by earthquakes, since 10 MPa is the global median stress drop associated with earthquakes (Allmann and Shearer, 2009).

In 2D models, plane strain is assumed. No discontinuity or weakness is introduced to represent the known faults, since we treat faults as stress indicators rather than stress-generating structures.

4.3.4. Post-processing

Principal stress orientations are calculated from total stress values whereas stress magnitudes are relative to the assumed lithostatic equilibrium state of

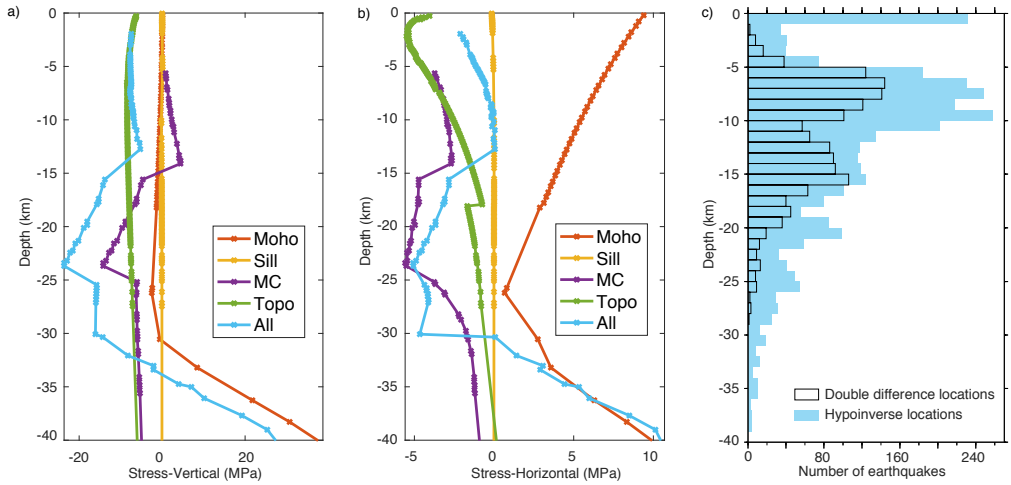

Figure 3: One-dimensional profiles from 2D static models. a) Vertical stresses along the 1D depth profile (green dashed line on Fig. 1c) with the stresses from a reference model subtracted. Initial stress state is assumed to be that of the reference model: a uniform-thickness three-layer model with no magmatic systems. Model values, marked with ×'s along the lines, are taken within 100 meters of the profile ($x = 2750$ m, where $x = 0$ is 36° longitude). Topo: topography model (Fig. 2d), Sill: sill model (Fig. 2e), MC: magma chamber model (Fig. 2f), Moho: thinned crust model (Fig. 2g), All: all-components model (Fig. 2h). b) Corresponding horizontal stresses along the 1D depth. c) Depth histogram of earthquakes in the study area from Weinstein et al. (2017).

the reference model (see Supplementary material SM5). The greatest compressive stress, σ_1, is taken as a proxy for preferred orientation of magmatic intrusions which is perpendicular to the preferred opening direction. The orientation of the least compressive stress (σ_3) is comparable to the T-axis of earthquake focal mechanisms or the regional extensional GNSS direction. Model results are viewed using the open-source visualization software ParaView 5.7.

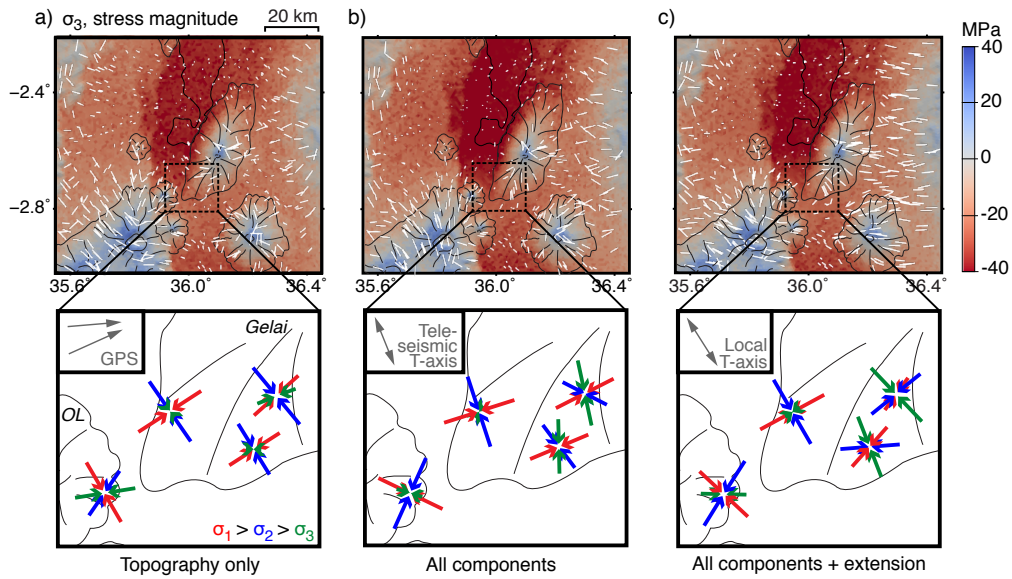

Figure 4: Depth slices of principal stresses in the upper crust (0–18 km depth) . These are 3D model results of a) topography only, b) all components together, c) all components together with extension. The top row are colored by stress magnitudes with white lines representing the least compressive stress orientations (σ_3), where dots represent a line coming off the page or vertical. The bottom row shows 3D principal stress orientations (projected to 2D onto the map) in the Naibor Soito region along with other stress markers from Fig. 1 on the top left corner for comparison. σ_1: greatest compressive stress; σ_2: intermediate compressive stress.

5. Results

5.1. Topography and validation of finite-element model

The 2D analytical model of topographic loading (Fig. 2c) reveals stress concentrations beneath the basin where sills or horizontal magma storage may be favored (greatest compressive stresses are horizontal) (e.g., Maccaferri et al., 2014). The corresponding numerical model (Fig. 2d) reveals similar patterns of stress concentrations but with smaller stress amplitudes, due to the material and domain constraints in the numerical model that do not exist in the half-space of the analytical model. The similarities between Figs. 2c and 2d help us validate the numerical model. In the analytical models, the effect of the lower-density basin fill is minimal (black vs. dashed red line on Fig. 2b are nearly coincident) hence the basin-fill density correction is not considered in succeeding models.

The topography-driven preferred region (shallow red areas in Figs. 2c,d) for melt storage beneath the basin is focused to a narrow region between the Natron rift flank on the west and the Gelai volcanic edifice on the east. The local topography creates a path of likely intrusion propagation (σ_1, black lines on Fig. 2) from beneath the basin towards the flanks of Gelai, similar to the models of off-rift volcanism of Maccaferri et al. (2014); that is, if there were magma at $\sim$10 km depth between OL and NS, it might intrude to shallower depths tracing along the σ_1 direction (black lines) towards Gelai to the east or towards OL to the west. This topographic loading effect is focused in the shallow crust, to a depth that scales with the length scale of the loading/unloading. For example, in the cross-section of the analytical 2D model (Fig. 2c), we see that the wide basin effect ($\sim$80 km wide) reaches 40

km depth, although the highest stresses due to the topographic depression between the border fault and Gelai (∼15 km wide) are limited to <20 km depth. On Fig. 3a, we observe that vertical strain due to topography peaks at ∼10 km depth. The lateral shift from zero of the entire topographic effect profile is arbitrary and depends on the assumed height of the reference model, and so for example, we can shift the profile to the right such that topographic stress is zero at the base of unrifted crust (40 km thick) (e.g., Roman and Jaupart, 2014).

5.2. Subsurface magmatic system

Both the sill and magma chamber produce a similar principal stress pattern with near-vertical σ_1 above them, but the stresses are about an order of magnitude apart, mainly due to the difference in size and magma pressure. For the sill, the stress perturbation is only due to the density difference which produces an upwards buoyancy push, but the stress magnitude is very small compared to all the other components considered in the study (Fig. 2e). For the magma chamber, in addition to the buoyancy effect, inflation adds an outward-directed pressure (Fig. 2f). Vertical σ_1 above the magma bodies creates a possible pathway for magma to reach the surface, where diking may be preferred.

5.3. Thinned crust

High-density mantle material replaces stretched continental crust that is 470 kg/m^2 lighter, imposing a downward pull on the system proportional to the crustal thinning (Fig. 2g). Crustal thinning has a long wavelength (rift-width scale) thereby affecting a larger region of the model, compared to the

high-frequency spatial variation of topography and smaller size of the magma bodies. The vertical σ_1 beneath the crust and horizontal σ_1 at the bottom of the crust suggest that stresses induced by crustal thinning may facilitate ponding of mafic magma around the Moho (e.g., Thybo and Artemieva, 2013; Maccaferri et al., 2014).

5.4. All components in 2D models

After testing each component separately, we create a model with all the components – topography, magma chamber, sill. Without extension (Fig. 2h), the 2D model has the recognizable stress patterns produced by the thinned crust, the inflated magma chamber, and the topography. Adding extension (Fig. 2i) noticeably changes the orientations of the greatest compressive stress. At shallow depths just beneath the Naibor Soito monogenetic cone complex and Gelai volcano, σ_1 is vertical, where it was near-horizontal without extension, suggesting that the large-scale heterogeneities (Moho, magma chamber, topography) facilitate localization of extensional stress and indicating the importance of taking into consideration the regional extensional setting in models.

On a one-dimensional profile of vertical stress (Fig. 3a), topography has the largest effect close to the surface, showing negative stresses in our models since topography at the location is below zero, hence lower than the reference model. The magma chamber inflation has a large effect near the magma chamber but becomes negligible within a few km distance farther away (Roman and Jaupart, 2014). The sill effect is negligible. The thinned crust imposes a large stress at the bottom of the crust that gradually decreases towards the surface. The horizontal stresses are smaller than the vertical

stresses, except for the rift-wide effect of the thinned crust which introduces a horizontal stress that is comparable to the vertical stresses. However when extension is added to the system, the effect of the thinned crust on the horizontal stresses close to the surface is lessened, as also observed in Fig. 2i.

5.5. Stress orientations in 3D

The similarity between principal stress orientations due to topography only (Fig. 4a) and all components (Fig. 4b) suggests that either 1) topography exerts the dominant stress field in the shallow upper crust, or 2) the most dominant stress-generating mechanisms considered contribute similarly-oriented stresses, especially away from southern Gelai and the Ngorongoro crater region. Beneath Lake Natron, σ_3 is near-vertical, and is probably mainly controlled by basin topography and crustal thinning.

On the southern flank of Gelai, topography alone without extension produces a stress field with σ_3 oriented NE–SW (Fig. 4a). Adding the subsurface effects, the direction of σ_3 becomes roughly N-S in southern Gelai (Fig. 4b), and with extension the σ_3 orients close to NW–SE (Fig. 4c), which is consistent with the local extensional (T-axis) direction in previous seismicity studies (Reiss et al., 2021; Weinstein et al., 2017). The agreement with local stress rotation observed from the recent local seismicity studies as well as teleseismically-detected earthquakes since 1964 in the Global Centroid Moment Tensor catalog suggest that subsurface effects and extension play an important role in the crustal state-of-stress.

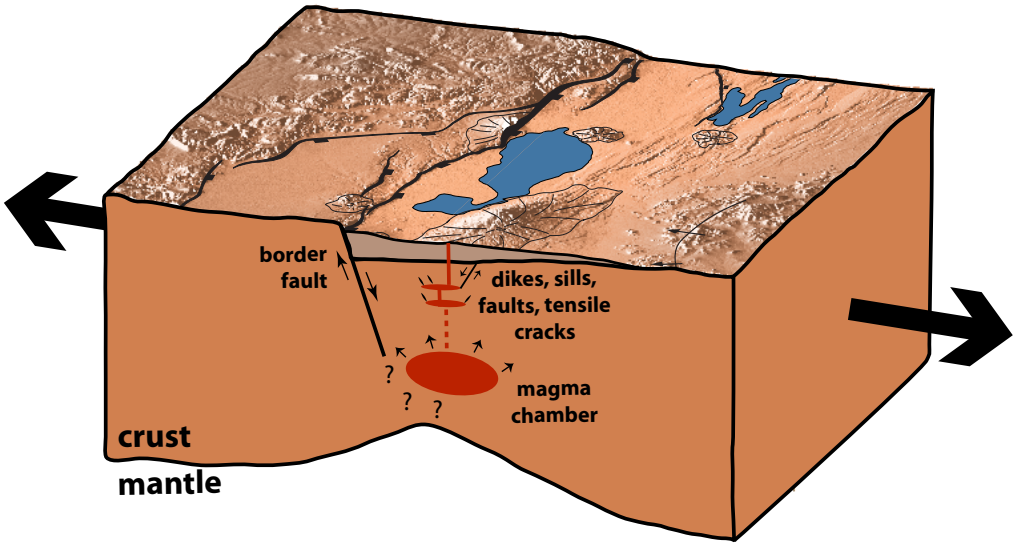

Figure 5: Schematic diagram of early-stage rifting. In addition to topographic loading, the subsurface density gradients from a thinned crust and the crustal magmatic complex also alter the stress field at depth. GNSS measurements constrain surface motions but do not represent strain at depth; they measure surface displacements. Thus, they are most sensitive to shallow stress fields and not deeper processes unless of greater magnitude, and generally are too sparse to provide information on deeper processes. Seismicity provides a better constraint on the stress field (strain field) at depth. Among the rift components considered in this study, surface topography and extension influences the shallow stress field the most (∼upper crust), but at depth (∼lower crust), subsurface density contrasts play a larger role. These large subsurface stresses may be overlooked when only considering surface-motion constraints but are key to a holistic three-dimensional understanding of rift tectonics.

6. Discussion

6.1. Three-dimensional rift tectonics

Stresses vary with depth, notably near-surface stresses differ from that of the rest of the upper crust and the lower crust (Fig. 3a,b). We note that topography has a significant influence on shallow vertical stresses, but subsurface components strongly affect deeper stresses and these cannot be ignored (Fig. 5). Surface observations, such as GNSS and Interferometric Synthetic Aperture Radar (InSAR) data, and surface lineaments, are most sensitive to shallow stress fields and not deeper processes except those of greater magnitude. Hence, considering only surface constraints on plate motion paints a two-dimensional picture of rifting that underestimates subsurface stress controls on the system. In addition, at the shallow level there are sedimentary basins that provide complexity through additional processes such as compaction, dewatering, and fluid overpressure. These processes influence near-surface stress fields, which factor in strongly in near-surface observations, but may not be representative of deeper, regional, tectonic-level processes. Most of the earthquakes in the study region are in the upper crust, from 5–15 km depths (Weinstein et al., 2017) (Fig. 3c), and hence provide stress constraints at depth, which are highly complementary with surface observations.

6.2. Rift evolution and strain transfer

Border faults form very early during rift initiation and may reach a maximum length largely determined by the thickness of strong lithosphere (e.g., Jackson and Blenkinsop, 1997; Ebinger et al., 1999). New faults, called transfer faults, may form to link initially discrete border faults and rift segments

into a contiguous system. Results of this study suggest that local changes in the stress field caused by the topographic loads, presence of crustal magma reservoirs, and evolution of crustal stretching within the system determine the orientation and evolution of these transfer fault systems. The local stress field influences where magmatism develops. For example, intrabasinal volcanic centers form in the high-strain accommodation zone. But it is important to note that once the magmatic systems are formed, they in turn impose their own stresses on the region and provide a local stress control where new faults and magmatic systems might develop, creating a feedback loop. Hence, geometric rift segment linkage models that do not consider the magmatic system (e.g., Acocella et al., 2005) may not be applicable in some magmatic rift zones.

The Natron basin sits at a transition zone, between the Kenya rift to the north which has central volcanoes along the rift axis, and the study region where there are no central rift volcanoes. In the Magadi basin, intra-rift faults accommodate 67–80% of regional extension, whereas in the Natron basin, the border faults accommodate >69% of the extension (Muirhead et al., 2016). The local changes to the stress field in the Natron area can guide fluids that move up the plate and could be indicative of the mechanism by which strain begins to localize intra-rift to the central depression during early-stage rifting. The ∼10-km crustal thinning imposes the largest stresses, especially horizontal stresses, but the feature generally follows the rift axis and so it cannot produce a local stress rotation (see Supplementary material Fig. SM2). Instead, the local stress rotation could be produced by the interplay between the volcanic edifices and the subsurface magmatic system.

The distribution and presence of magma within the crust contributes more to stresses at depth, whereas the loading effect of volcanic edifices is largest at shallow depths. The magmatic system (surface and subsurface) induces a local stress field rotation that might allow extensional faults or dikes to form at rift-oblique angles, which then later facilitate rift linkage between segmented basins and strain migration towards intra-rift faults where magma intrusion accommodates a larger percentage of extension.

7. Conclusions

Using physics-based numerical models, constrained by data and compared to analytical models, we explore the effects of different rift loading components on the crustal state-of-stress. Models suggest that a local stress field rotation to NW–SE extension (T-axis) from the regional ∼E-W extension (from GNSS) can be due to the combined top loading from topography and bottom loading from magma chamber inflation. We find that topographic loading governs shallow upper crustal stresses but subsurface components (magma bodies, crustal thinning) can strongly influence lower crustal stresses, which in turn may guide the location and upward path of magma intrusion. The magmatic system (surface and subsurface) in an early-stage rift provides a mechanism (local stress rotation) for later rift linkage between segmented basins and strain migration towards the central rift zone. Studies constrained only by surface observations underestimate stresses from crustal thinning and lower crustal magmatic systems. Inclusion of the internal and subsurface loads provides new insights into strain and magma migration during rift evolution.

8. Acknowledgements

This research was supported by Tulane University's Marshall-Heape endowment (CJE, SJO), Geological Society of America Student Research Grant (SJO), and Tulane University's Vokes Fellowship (SJO). We thank the Computational Infrastructure for Geodynamics (`http://geodynamics.org`) which is funded by the National Science Foundation under awards EAR-0949446 and EAR-1550901, for the PyLith software and tutorial workshops. CAW acknowledges support from Public Research Funding from the Government of New Zealand. ER received funding from the Deutsche Forschungsgemeinschaft (DFG – German Research Foundation), Grant Number RI 2782/2 (634756). Figures were created using Generic Mapping Tools v.5.4.5, ParaView 5.7, MATLAB, and Adobe Illustrator.

References

Aagaard, B., Knepley, M., Williams, C., 2017a. PyLith User Manual, Version 2.2.1. Computational Infrastructure for Geodynamics (CIG). University of California, Davis. URL: `https://geodynamics.org/cig/software/github/pylith/v2.2.1/pylith-2.2.1_manual.pdf`.

Aagaard, B., Knepley, M., Williams, C., 2017b. PyLith v2.2.1. Computational Infrastructure for Geodynamics (CIG). University of California, Davis. doi:`http://doi.org/10.5281/zenodo.886600`.

Aagaard, B.T., Knepley, M.G., Williams, C.A., 2013. A domain decomposition approach to implementing fault slip in finite-element models of quasi-

static and dynamic crustal deformation. Journal of Geophysical Research: Solid Earth 118, 3059–3079. doi:https://doi.org/10.1002/jgrb.50217.

Acocella, V., Morvillo, P., Funiciello, R., 2005. What controls relay ramps and transfer faults within rift zones? insights from analogue models. Journal of Structural Geology 27, 397–408. doi:https://doi.org/10.1016/j.jsg.2004.11.006.

Allmann, B.P., Shearer, P.M., 2009. Global variations of stress drop for moderate to large earthquakes. Journal of Geophysical Research: Solid Earth 114, 1–22. doi:https://doi.org/10.1029/2008JB005821.

Aulbach, S., Rudnick, R.L., McDonough, W.F., 2011. Evolution of the lithospheric mantle beneath the east african rift in tanzania and its potential signatures in rift magmas. Geological Society of America Special Papers 478, 105–125. doi:http://doi.org/10.1130/2011.2478(06).

Baer, G., Hamiel, Y., Shamir, G., Nof, R., 2008. Evolution of a magma-driven earthquake swarm and triggering of the nearby oldoinyo lengai eruption, as resolved by insar, ground observations and elastic modeling, east african rift, 2007. Earth and Planetary Science Letters 272, 339–352. doi:https://doi.org/10.1016/j.epsl.2008.04.052.

Biggs, J., Amelung, F., Gourmelen, N., Dixon, T.H., Kim, S.W., 2009. Insar observations of 2007 tanzania rifting episode reveal mixed fault and dyke extension in an immature continental rift. Geophysical Journal International 179, 549–558. doi:https://doi.org/10.1111/j.1365-246X.2009.04262.x.

Birt, C., Maguire, P., Khan, M., Thybo, H., Keller, G.R., Patel, J., 1997. The influence of pre-existing structures on the evolution of the southern kenya rift valley—evidence from seismic and gravity studies. Tectonophysics 278, 211–242. doi:https://doi.org/10.1016/S0040-1951(97)00105-4.

Brocher, T.M., 2005. Empirical relations between elastic wavespeeds and density in the earth's crust. Bulletin of the seismological Society of America 95, 2081–2092. doi:https://doi.org/10.1785/0120050077.

Calais, E., d'Oreye, N., Albaric, J., Deschamps, A., Delvaux, D., Déverchere, J., Ebinger, C., Ferdinand, R.W., Kervyn, F., Macheyeki, A.S., et al., 2008. Strain accommodation by slow slip and dyking in a youthful continental rift, east africa. Nature 456, 783. doi:https://doi.org/10.1038/nature07478.

Cashman, K.V., Sparks, R.S.J., Blundy, J.D., 2017. Vertically extensive and unstable magmatic systems: a unified view of igneous processes. Science 355, eaag3055. doi:http://doi.org/10.1126/science.aag3055.

Corti, G., Bonini, M., Sokoutis, D., Innocenti, F., Manetti, P., Cloetingh, S., Mulugeta, G., 2004. Continental rift architecture and patterns of magma migration: A dynamic analysis based on centrifuge models. Tectonics 23. doi:https://doi.org/10.1029/2003TC001561.

Dahm, T., 2000. Numerical simulations of the propagation path and the arrest of fluid-filled fractures in the earth. Geophysical Journal International 141, 623–638. doi:https://doi.org/10.1046/j.1365-246x.2000.00102.x.

Dawson, J., 1992. Neogene tectonics and volcanicity in the north tanzania sector of the gregory rift valley: contrasts with the kenya sector. Tectonophysics 204, 81–92. doi:https://doi.org/10.1016/0040-1951(92)90271-7.

Ebinger, C., Jackson, J., Foster, A., Hayward, N., 1999. Extensional basin geometry and the elastic lithosphere. Philosophical Transactions of the Royal Society of London. Series A: Mathematical, Physical and Engineering Sciences 357, 741–765. doi:https://doi.org/10.1098/rsta.1999.0351.

Ebinger, C.J., 1989. Geometric and kinematic development of border faults and accommodation zones, kivu-rusizi rift, africa. Tectonics 8, 117–133. doi:https://doi.org/10.1029/TC008i001p00117.

Foster, A., Ebinger, C., Mbede, E., Rex, D., 1997. Tectonic development of the northern tanzanian sector of the east african rift system: Journal of the geological society of london, v. 154. doi 10, 689–700. doi:https://doi.org/10.1144/gsjgs.154.4.0689.

Guerri, M., Cammarano, F., Connolly, J.A., 2015. Effects of chemical composition, water and temperature on physical properties of continental crust. Geochemistry, Geophysics, Geosystems 16, 2431–2449. doi:https://doi.org/10.1002/2015GC005819.

Jackson, J., Blenkinsop, T., 1997. The bilila-mtakataka fault in malaŵi: An active, 100-km long, normal fault segment in thick seismogenic crust. Tectonics 16, 137–150. doi:https://doi.org/10.1029/96TC02494.

Jarvis, A., Reuter, H.I., Nelson, A., Guevara, E., 2008. Hole-filled srtm for the globe version 4, available from the cgiar-csi srtm 90m database. URL: http://srtm.csi.cgiar.org/.

Karlstrom, L., Dufek, J., Manga, M., 2009. Organization of volcanic plumbing through magmatic lensing by magma chambers and volcanic loads. Journal of Geophysical Research: Solid Earth 114. doi:https://doi.org/10.1029/2009JB006339.

Kervyn, M., Ernst, G., van Wyk de Vries, B., Mathieu, L., Jacobs, P., 2009. Volcano load control on dyke propagation and vent distribution: Insights from analogue modeling. Journal of Geophysical Research: Solid Earth 114. doi:https://doi.org/10.1029/2008JB005653.

King, R., Floyd, M., Reilinger, R., Bendick, R., 2019. Gps velocity field (mit 2019.0) for the east african rift system generated by king et al. URL: http://doi.iedadata.org/324785, doi:http://doi.org/10.1594/IEDA/324785.

Larsen, H., 1988. A multiple and propagating rift model for the ne atlantic. Geological Society, London, Special Publications 39, 157–158. doi:http://doi.org/10.1144/GSL.SP.1988.039.01.15.

Le Gall, B., Nonnotte, P., Rolet, J., Benoit, M., Guillou, H., Mousseau-Nonnotte, M., Albaric, J., Déverchère, J., 2008. Rift propagation at craton margin.: Distribution of faulting and volcanism in the north tanzanian divergence (east africa) during neogene times. Tectonophysics 448, 1–19. doi:https://doi.org/10.1016/j.tecto.2007.11.005.

Maccaferri, F., Rivalta, E., Keir, D., Acocella, V., 2014. Off-rift volcanism in rift zones determined by crustal unloading. Nature Geoscience 7, 297. doi:https://doi.org/10.1038/ngeo2110.

Magee, C., Muirhead, J.D., Karvelas, A., Holford, S.P., Jackson, C.A., Bastow, I.D., Schofield, N., Stevenson, C.T., McLean, C., McCarthy, W., et al., 2016. Lateral magma flow in mafic sill complexes. Geosphere 12, 809–841. doi:https://doi.org/10.1130/GES01256.1.

Mana, S., Furman, T., Turrin, B.D., Feigenson, M.D., Swisher III, C.C., 2015. Magmatic activity across the east african north tanzanian divergence zone. Journal of the Geological Society 172, 368–389. doi:https://doi.org/10.1144/jgs2014-072.

Mansur, A.T., Manya, S., Timpa, S., Rudnick, R.L., 2014. Granulite-facies xenoliths in rift basalts of northern tanzania: age, composition and origin of archean lower crust. Journal of Petrology 55, 1243–1286. doi:https://doi.org/10.1093/petrology/egu024.

McHenry, L.J., Luque, L., Gómez, J.Á., Diez-Martín, F., 2011. Promise and pitfalls for characterizing and correlating the zeolitically altered tephra of the pleistocene peninj group, tanzania. Quaternary Research 75, 708–720. doi:https://doi.org/10.1016/j.yqres.2010.11.008.

Muirhead, J., Kattenhorn, S., Lee, H., Mana, S., Turrin, B., Fischer, T., Kianji, G., Dindi, E., Stamps, D., 2016. Evolution of upper crustal faulting assisted by magmatic volatile release during early-stage continental rift

development in the east african rift. Geosphere 12, 1670–1700. doi:https://doi.org/10.1130/GES01375.1.

Muirhead, J.D., Kattenhorn, S.A., Le Corvec, N., 2015. Varying styles of magmatic strain accommodation across the east african rift. Geochemistry, Geophysics, Geosystems 16, 2775–2795. doi:https://doi.org/10.1002/2015GC005918.

Oliva, S., Ebinger, C., Wauthier, C., Muirhead, J., Roecker, S., Rivalta, E., Heimann, S., 2019. Insights into fault-magma interactions in an early-stage continental rift from source mechanisms and correlated volcano-tectonic earthquakes. Geophysical Research Letters 46, 2065–2074. doi:https://doi.org/10.1029/2018GL080866.

Plasman, M., Tiberi, C., Ebinger, C., Gautier, S., Albaric, J., Peyrat, S., Deverchere, J., Le Gall, B., Tarits, P., Roecker, S., et al., 2017. Lithospheric low-velocity zones associated with a magmatic segment of the tanzanian rift, east africa. Geophysical Journal International 210, 465–481. doi:https://doi.org/10.1093/gji/ggx177.

Pollard, D., 1987. Elementary fracture mechanics applied to the structural interpretation of dykes, in: Halls, H.C., Fahrig, W.F. (Eds.), Mafic Dyke Swarms. Geol. Assoc. of Can.. volume 34, pp. 112–128.

Reiss, M., Muirhead, J., Laizer, A., Link, F., Kazimoto, E., Ebinger, C., Rümpker, G., 2021. The impact of complex volcanic plumbing on the nature of seismicity in the developing magmatic natron rift, tanzania.

front. Earth Sci 8, 609805. doi:https://doi.org/10.3389/feart.2020.609805.

Rivalta, E., Corbi, F., Passarelli, L., Acocella, V., Davis, T., Di Vito, M.A., 2019. Stress inversions to forecast magma pathways and eruptive vent location. Science advances 5, eaau9784. doi:https://doi.org/10.1126/sciadv.aau9784.

Roecker, S., Ebinger, C., Tiberi, C., Mulibo, G., Ferdinand-Wambura, R., Mtelela, K., Kianji, G., Muzuka, A., Gautier, S., Albaric, J., et al., 2017. Subsurface images of the eastern rift, africa, from the joint inversion of body waves, surface waves and gravity: investigating the role of fluids in early-stage continental rifting. Geophysical Journal International 210, 931–950. doi:https://doi.org/10.1093/gji/ggx220.

Roman, A., Jaupart, C., 2014. The impact of a volcanic edifice on intrusive and eruptive activity. Earth and Planetary Science Letters 408, 1–8. doi:https://doi.org/10.1016/j.epsl.2014.09.016.

Saria, E., Calais, E., Stamps, D., Delvaux, D., Hartnady, C., 2014. Present-day kinematics of the east african rift. Journal of Geophysical Research: Solid Earth 119, 3584–3600. doi:https://doi.org/10.1002/2013JB010901.

Sibson, R.H., 1985. A note on fault reactivation. Journal of Structural Geology 7, 751–754. doi:https://doi.org/10.1016/0191-8141(85)90150-6.

Smith, M., Mosley, P., 1993. Crustal heterogeneity and basement influence

on the development of the kenya rift, east africa. Tectonics 12, 591–606. doi:https://doi.org/10.1029/92TC01710.

Thybo, H., Artemieva, I.M., 2013. Moho and magmatic underplating in continental lithosphere. Tectonophysics 609, 605–619. doi:https://doi.org/10.1016/j.tecto.2013.05.032.

Tibaldi, A., Bonali, F.L., Pasquaré Mariotto, F., Corti, N., Russo, E., Einarsson, P., Hjartardóttir, Á.R., 2020. Rifting kinematics produced by magmatic and tectonic stresses in the north volcanic zone of iceland. Frontiers in Earth Science 8, 174. doi:https://doi.org/10.3389/feart.2020.00174.

Tiberi, C., Gautier, S., Ebinger, C., Roecker, S., Plasman, M., Albaric, J., Déverchère, J., Peyrat, S., Perrot, J., Wambura, R.F., et al., 2018. Lithospheric modification by extension and magmatism at the craton-orogenic boundary: North tanzania divergence, east africa. Geophysical Journal International 216, 1693–1710. doi:https://doi.org/10.1093/gji/ggy521.

Tugume, F., Nyblade, A., Julià, J., 2012. Moho depths and poisson's ratios of precambrian crust in east africa: evidence for similarities in archean and proterozoic crustal structure. Earth and Planetary Science Letters 355, 73–81. doi:https://doi.org/10.1016/j.epsl.2012.08.041.

Wadge, G., Biggs, J., Lloyd, R., Kendall, J.M., 2016. Historical volcanism and the state of stress in the east african rift system. Frontiers in Earth Science 4, 86. doi:https://doi.org/10.3389/feart.2016.00086.

Weinstein, A., Oliva, S.J., Ebinger, C., Roecker, S., Tiberi, C., Aman, M., Lambert, C., Witkin, E., Albaric, J., Gautier, S., et al., 2017. Fault-magma interactions during early continental rifting: Seismicity of the m agadi-n atron-m anyara basins, a frica. Geochemistry, Geophysics, Geosystems 18, 3662–3686. doi:https://doi.org/10.1002/2017GC007027.

Supplementary material of

State of stress and stress rotations: Quantifying the role of surface topography and subsurface density contrasts in magmatic rift zones (Eastern Rift, Africa)

S. J. Oliva, C. J. Ebinger, E. Rivalta, C. A. Williams, C. Wauthier, C. Currie

Contents of this file:

SM1 Figure: Gravitational stresses due to reference model
SM2 Figure: Map view of stresses due to crustal thinning
SM3 Trelis input for 2D and 3D model geometry and meshing
SM4 General PyLith parameters (pylithapp.cfg)
SM5 Post-processing calculations

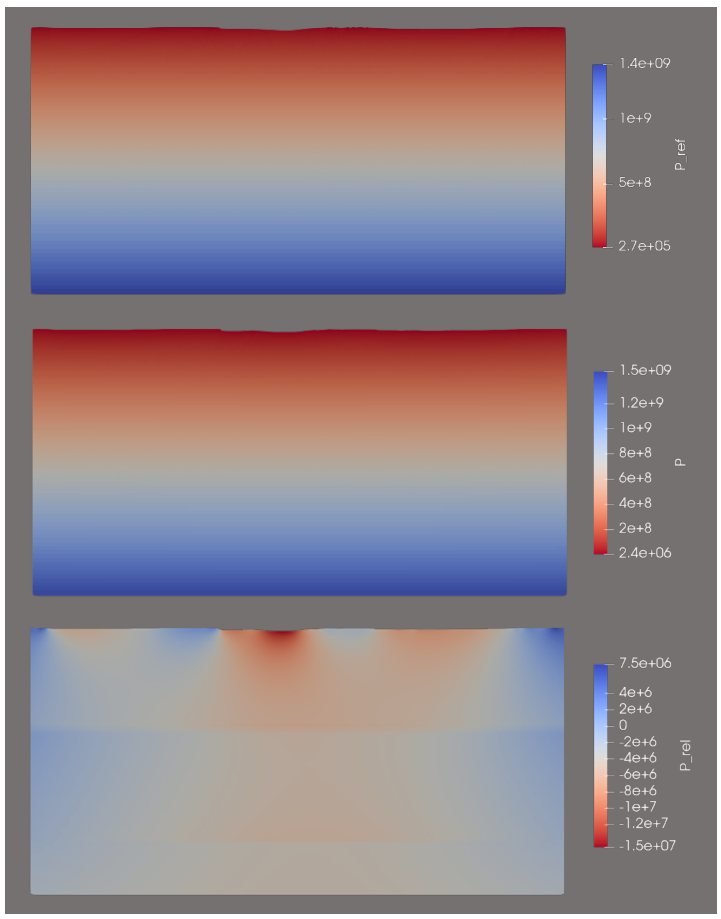

Figure SM1. The top figure (P_ref) shows the gravitational stresses of the reference model, a uniform-thickness three-layer model with no magmatic systems. The middle figure (P) shows the stresses due to topography – note that the gravitational stresses dominate and obscure any stress patterns due to topography. Hence, we subtract the assumed initial stress state corresponding to the reference model (P_ref) from our models of different components (P) to obtain the stress

patterns that we interpret in the figure (P_rel, bottom figure). All three figures have color bars scaled to the data range. The bottom figure is equivalent to Fig. 2d, but in the main text all color bars are centered at zero.

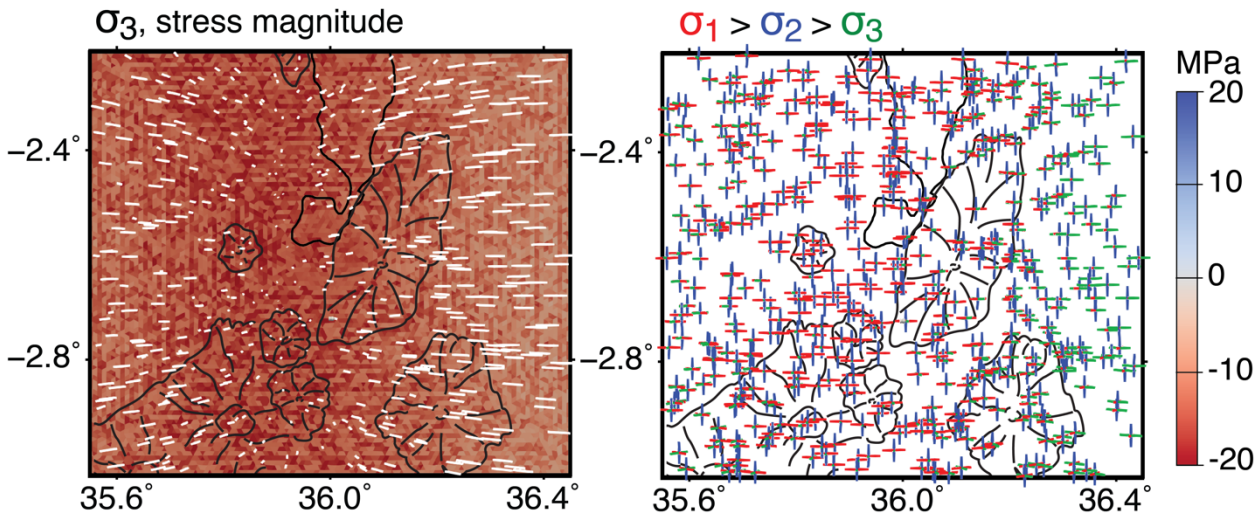

Figure SM2. 3D modeling of crustal thinning: Left panel is colored by stress magnitude with while lines representing the least compressive stress orientations (sigma 3), where dots represent a line coming off the page or vertical. Right panel shows the 3D principal stress orientations, projected to 2D onto the map. Note that sigma 1 is oriented E-W, sigma 2 is N-S, and sigma 3 is near-vertical along the rift basin. With the principal stress orientations generally aligned rift-parallel, rift-perpendicular, and vertical, we conclude that the crustal thinning cannot produce the map-view 60-degree local stress rotation observed from focal mechanisms.

SM3. Geometry and Mesh

Below we include the Trelis codes (.jou) to create the geometry and build the mesh of the complete model that includes all components (topography, moho, sill, magma chamber) in 2D and 3D.

```
# 2D Geometry
# ----------------------------------------------------------------------
# -*- Python -*- (syntax highlighting)
# ----------------------------------------------------------------------
reset
${Units('si')}

# ----------------------------------------------------------------------
# Import Topo and Moho curves
# ----------------------------------------------------------------------
import Acis "curve_moho.sat"
import Acis "curve_topo_272_100m_detrendzero.sat"

# ----------------------------------------------------------------------
# Create surface using vertices
# ----------------------------------------------------------------------

${domainW=300.0*km}
${domainH=110.0*km}
```

```
create vertex {-0.5*domainW} {-domainH+10.0*km}  0.0
${idVSbegin=Id("vertex")}
create vertex {-0.5*domainW} {10.0*km}  0.0
create vertex {+0.5*domainW} {10.0*km}  0.0
create vertex {+0.5*domainW} {-domainH+10.0*km}  0.0
${idVSend=Id("vertex")}
create surface vertex {idVSbegin} to {idVSend}

# ---------------------------------------------------------------------
# Create material interface surfaces
# ---------------------------------------------------------------------

# Magma chamber
create vertex {5.5*km} {-20.0*km} 0.0
${idVCirc=Id("vertex")}
create curve arc center vertex {idVCirc} radius {10.0*km} full
curve 7 name "chamber"
surface chamber scale x 1 y 0.5 about {5.5*km} {-20*km}
imprint surface 1 with curve chamber

# Constant thickness crust
${ucrustD=18.0*km}
create vertex {-0.5*domainW} {-ucrustD}  0.0
${idVM1=Id("vertex")}
create vertex {+0.5*domainW} {-ucrustD}  0.0
${idVM2=Id("vertex")}
create curve vertex {idVM1} vertex {idVM2} on surface 2
imprint surface 2 with curve 9

# Split across Moho curve
split curve 17 crossing curve moho
split curve 18 crossing curve moho
imprint surface 5 with curve moho

# Split across topo curve
split curve 11 crossing curve topo
split curve 12 crossing curve topo
imprint surface 4 with curve topo
delete surface 8

# Sill complex
create vertex {0.0*km} {-7.0*km} 0.0
${idVertex1=Id("vertex")}
create vertex {2.5*km} {-6.75*km} 0.0
${idVertex2=Id("vertex")}
create vertex {2.5*km} {-7.0*km} 0.0
${idVertex3=Id("vertex")}
create curve vertex {idVertex1} vertex {idVertex2} vertex {idVertex3} ellipse first
angle 0 last angle 360
curve 29 name "sill"
imprint surface 9 with curve sill

surface 11 name "s_ucrust"
surface 6 name "s_lcrust"
surface 7 name "s_mantle"
surface 10 name "s_sill"
surface 3 name "s_chamber"

# ---------------------------------------------------------------------
# Name geometric entities for use in meshing.
# ---------------------------------------------------------------------

curve 28 name "c_topo"
#curve 6 name "c_conrad"
#curve 15 name "c_moho"
```

```
curve 6 name "c_bottom"

curve 30 name "c_sill"
curve 14 name "c_chambertop"
curve 15 name "c_chamberbottom"
curve 16 name "c_chamberright"

curve 24 name "c_ucrust_xneg"
curve 27 name "c_ucrust_xpos"
curve 22 name "c_lcrust_xneg"
curve 19 name "c_lcrust_xpos"
curve 21 name "c_mantle_xneg"
curve 20 name "c_mantle_xpos"

delete vertex all

# End of file
```

```
# 2D Mesh
# ----------------------------------------------------------------------
# -*- Python -*- (syntax highlighting)
# ----------------------------------------------------------------------

# ----------------------------------------------------------------------
# Set discretization size
# ----------------------------------------------------------------------
surface all size {1.0*km}
surface s_sill size {0.2*km}
surface s_chamber size {0.5*km}
surface s_ucrust size {0.5*km}
surface s_lcrust size {0.5*km}
surface s_mantle size {0.8*km}

# ----------------------------------------------------------------------
# Generate the mesh
# ----------------------------------------------------------------------
delete mesh
surface all scheme pave
mesh surface all

# ----------------------------------------------------------------------
# Smooth mesh to improve quality
# ----------------------------------------------------------------------
surface all smooth scheme condition number beta 1.3 cpu 10
smooth surface all

# ----------------------------------------------------------------------
# Create blocks for materials
# ----------------------------------------------------------------------
block 1 surface s_ucrust
block 1 name "ucrust"

block 2 surface s_lcrust
block 2 name "lcrust"

block 3 surface s_mantle
block 3 name "mantle"

block 4 surface s_sill
block 4 name "sill"

block 5 surface s_chamber
block 5 name "chamber"
```

```
# ----------------------------------------------------------------------
# Create nodeset for +x edge
# ----------------------------------------------------------------------
group "boundary_xpos" add node in curve c_ucrust_xpos
group "boundary_xpos" add node in curve c_lcrust_xpos
group "boundary_xpos" add node in curve c_mantle_xpos
nodeset 20 group boundary_xpos
nodeset 20 name "boundary xpos"

# ----------------------------------------------------------------------
# Create nodeset for -x edge
# ----------------------------------------------------------------------
group "boundary_xneg" add node in curve c_ucrust_xneg
group "boundary_xneg" add node in curve c_lcrust_xneg
group "boundary_xneg" add node in curve c_mantle_xneg
nodeset 21 group boundary_xneg
nodeset 21 name "boundary xneg"

# ----------------------------------------------------------------------
# Create nodeset for +y edge
# ----------------------------------------------------------------------
group "boundary_ypos" add node in curve  c_topo
nodeset 22 group boundary_ypos
nodeset 22 name "boundary ypos"

# ----------------------------------------------------------------------
# Create nodeset for -y edge
# ----------------------------------------------------------------------
group "boundary_yneg" add node in curve  c_bottom
nodeset 23 group boundary_yneg
nodeset 23 name "boundary yneg"

# ----------------------------------------------------------------------
# Create nodeset for sill complex
# ----------------------------------------------------------------------
group "boundary_sill" add node in curve c_sill
nodeset 24 group boundary_sill
nodeset 24 name "boundary sill"

# ----------------------------------------------------------------------
# Create nodeset for magma chamber
# ----------------------------------------------------------------------
group "boundary_chamber" add node in curve c_chambertop
group "boundary_chamber" add node in curve c_chamberbottom
group "boundary_chamber" add node in curve c_chamberright
nodeset 25 group boundary_chamber
nodeset 25 name "boundary chamber"

# ----------------------------------------------------------------------
# Export exodus file
# ----------------------------------------------------------------------
export mesh "mesh_2d_mod6.exo" dimension 2 overwrite

# End of file
```

```
# 3D Geometry
# ----------------------------------------------------------------------
# -*- Python -*- (syntax highlighting)
# ----------------------------------------------------------------------
reset
${Units('si')}

# ----------------------------------------------------------------------
# Create block
```

```
# ----------------------------------------------------------------------
# Block is 250 km x 500 km x 62 km
${blockLength=200.0*km}
${blockWidth=190.0*km}
${blockHeight=110.0*km}

brick x {blockLength} y {blockWidth} z {blockHeight}
${idVol=Id("volume")}

# Translate block so top can be chopped with topography and so faults
# intersect upper surface rather than side.
${moveX=0.0*km}
${moveY=13.0*km} #topo centered at 2.72 S
#volume {idVol} move x {moveX} y {moveY} z {0.0*km}
volume {idVol} move x {moveX} y {moveY} z {-0.5*blockHeight+10.0*km}

# ----------------------------------------------------------------------
# Import topography.
# ----------------------------------------------------------------------
import Acis "srtm_1km_detrend/crafti_topo_detrend.sat"

# Scale topo, 1 km = 1000 m
surface 7 scale 1000
#save
# ----------------------------------------------------------------------
# Webcut block with topography and delete volume lying above topography.
# ----------------------------------------------------------------------
webcut volume {idVol} with sheet surface 7
delete volume 3
delete body 2
#save
# ----------------------------------------------------------------------
# Divide upper crust, lower crust, and mantle
# ----------------------------------------------------------------------
create planar surface with plane zplane offset {-18.0*km}
webcut volume 1 with sheet surface 18

# Magma chamber
create sphere radius {5*km}
${idSphere=Id("volume")}
volume {idSphere} move x {5.5*km} y 0 z {-20*km}
volume {idSphere} scale x 2 y 2 z 1 about {5.5*km} 0 {-20*km}

subtract volume 6 from volume 1 imprint keep
subtract volume 6 from volume 5 imprint keep
delete volume 1 5

# Sill
create sphere radius {0.5*km}
${idSphere=Id("volume")}
volume {idSphere} move x {2.5*km} y 0 z {-7*km}
volume {idSphere} scale x 10 y 10 z 1 about {2.5*km} 0 {-7*km}

subtract volume 9 from volume 7 imprint keep
delete volume 7

# Moho
import Acis "curve_moho_3d.sat"
curve moho move x 0 y {-90*km} z 0
webcut volume 8 sweep curve moho vector 0 1 0 distance {220*km}

delete body 4
delete curve moho
```

```
imprint all with volume all
merge all
delete vertex all

# ----------------------------------------------------------------------
# Name geometric entities for use in meshing.
# ----------------------------------------------------------------------

surface 49 name "topo"
surface 38 name "conrad"
surface 53 name "moho"
surface 43 name "sbottom"
surface 45 name "chambertop"
surface 37 name "chamberbottom"
surface 44 name "sill_surf"

volume 10 name "ucrust"
volume 8 name "lcrust"
volume 11 name "mantle"
volume 6 name "chamber"
volume 9 name "sill"

surface 50 name "ucrust_ypos"
surface 51 name "ucrust_xneg"
surface 47 name "ucrust_yneg"
surface 48 name "ucrust_xpos"

surface 56 name "lcrust_yneg"
surface 57 name "lcrust_xpos"
surface 54 name "lcrust_ypos"
surface 55 name "lcrust_xneg"

surface 61 name "mantle_yneg"
surface 62 name "mantle_xneg"
surface 59 name "mantle_ypos"
surface 60 name "mantle_xpos"

# End of file
```

```
# 3D Mesh
# ----------------------------------------------------------------------
# -*- Python -*- (syntax highlighting)
# ----------------------------------------------------------------------

# ----------------------------------------------------------------------
# Set discretization size
# ----------------------------------------------------------------------
surface topo size {1.0*km}
surface conrad size {2.5*km}
surface moho size {5.0*km}
surface sbottom size {10.0*km}
surface chambertop size {1.0*km}
surface chamberbottom size {1.0*km}
surface sill_surf size {0.2*km}

# Sizing functions for faces surrounding upper crust.
surface ucrust_xneg sizing function type bias start curve 95 finish curve 71
surface ucrust_xpos sizing function type bias start curve 93 finish curve 73
surface ucrust_yneg sizing function type bias start curve 90 finish curve 72
surface ucrust_ypos sizing function type bias start curve 94 finish curve 70

# Sizing functions for faces surrounding lower crust.
surface lcrust_xneg sizing function type bias start curve 71 finish curve 100
surface lcrust_xpos sizing function type bias start curve 73 finish curve 102
```

```
surface lcrust_yneg sizing function type bias start curve 72 finish curve 99
surface lcrust_ypos sizing function type bias start curve 70 finish curve 101

# Sizing functions for faces surrounding mantle.
surface mantle_xneg sizing function type bias start curve 100 finish curve 78
surface mantle_xpos sizing function type bias start curve 102 finish curve 81
surface mantle_yneg sizing function type bias start curve 99 finish curve 75
surface mantle_ypos sizing function type bias start curve 101 finish curve 80

# ----------------------------------------------------------------------
# Generate the mesh
# ----------------------------------------------------------------------
delete mesh
volume all scheme tetmesh
mesh surface topo
mesh surface all except topo
mesh volume all

# ----------------------------------------------------------------------
# Smooth mesh to improve quality
# ----------------------------------------------------------------------
volume all smooth scheme condition number beta 2.0 cpu 3
smooth volume all

# ----------------------------------------------------------------------
# Create blocks for materials
# ----------------------------------------------------------------------
block 1 volume ucrust
block 1 name "ucrust"

block 2 volume lcrust
block 2 name "lcrust"

block 3 volume mantle
block 3 name "mantle"

block 4 volume sill
block 4 name "sill"

block 5 volume chamber
block 5 name "chamber"

# ----------------------------------------------------------------------
# Create nodeset for +x edge
# ----------------------------------------------------------------------
group "boundary_xpos" add node in surface ucrust_xpos
group "boundary_xpos" add node in surface lcrust_xpos
group "boundary_xpos" add node in surface mantle_xpos
nodeset 30 group boundary_xpos
nodeset 30 name "boundary_xpos"

# ----------------------------------------------------------------------
# Create nodeset for -x edge
# ----------------------------------------------------------------------
group "boundary_xneg" add node in surface ucrust_xneg
group "boundary_xneg" add node in surface lcrust_xneg
group "boundary_xneg" add node in surface mantle_xneg
nodeset 31 group boundary_xneg
nodeset 31 name "boundary_xneg"

# ----------------------------------------------------------------------
# Create nodeset for +y edge
# ----------------------------------------------------------------------
group "boundary_ypos" add node in surface ucrust_ypos
group "boundary_ypos" add node in surface lcrust_ypos
```

```
group "boundary_ypos" add node in surface mantle_ypos
nodeset 32 group boundary_ypos
nodeset 32 name "boundary_ypos"

# ----------------------------------------------------------------------
# Create nodeset for -y edge
# ----------------------------------------------------------------------
group "boundary_yneg" add node in surface ucrust_yneg
group "boundary_yneg" add node in surface lcrust_yneg
group "boundary_yneg" add node in surface mantle_yneg
nodeset 33 group boundary_yneg
nodeset 33 name "boundary_yneg"

# ----------------------------------------------------------------------
# Create nodeset for +z edge
# ----------------------------------------------------------------------
group "boundary_zpos" add node in surface topo
nodeset 34 group boundary_zpos
nodeset 34 name "boundary_zpos"

# ----------------------------------------------------------------------
# Create nodeset for -z edge
# ----------------------------------------------------------------------
group "boundary_zneg" add node in surface sbottom
nodeset 35 group boundary_zneg
nodeset 35 name "boundary_zneg"

# ----------------------------------------------------------------------
# Create nodeset for sill
# ----------------------------------------------------------------------
group "boundary_sill" add node in surface sill_surf
nodeset 36 group boundary_sill
nodeset 36 name "boundary_sill"

# End of file
```

SM4. General PyLith parameters

Below is the pylithapp.cfg file used in 2D and 3D models.

```
# PyLith parameters for 2D models

# The settings in this file (pylithapp.cfg) will be read automatically
# by pylith, as long as the file is placed in the run directory.

# The settings in this file will override any settings in:
# PREFIX/etc/pylithapp.cfg
# $HOME/.pyre/pylithapp/pylithapp.cfg

# The settings in this file will be overridden by any .cfg file given
# on the command line or by any command line settings.

[pylithapp]

# ----------------------------------------------------------------------
# journal
# ----------------------------------------------------------------------
# The settings below turn on journal info for the specified components.
# If you want less output to stdout, you can turn these off.
[pylithapp.journal.info]
timedependent = 1
```

```
implicit = 1
petsc = 1
solverlinear = 1
meshiocubit = 1
homogeneous = 1
elasticityimplicit = 1
fiatlagrange = 1
pylithapp = 1
materials = 1

# ----------------------------------------------------------------------
# mesh_generator
# ----------------------------------------------------------------------
# The settings below control the mesh generation (importing mesh info).
# Turn on debugging output for mesh generation.
[pylithapp.mesh_generator]
debug = 1
reader = pylith.meshio.MeshIOCubit

# This component specification means we are using PyLith ASCII format,
# and we then specify the filename and number of space dimensions for
# the mesh.
[pylithapp.mesh_generator.reader]
filename = mesh/mesh_2d_mod1.exo
coordsys.space_dim = 2

# ----------------------------------------------------------------------
# problem
# ----------------------------------------------------------------------
# Specify the problem settings.
# This is a time-dependent problem, so we select this as our problem type.
# We select a total time of 0 sec, and a time step size of 1 sec, so we
# are performing a single time step.
# The spatial dimension for this problem is 2.
# For an implicit formulation (using implicit.cfg), we will perform 1
# implicit time step from t = -1.0 to t = 0.0 (elastic solution step).
[pylithapp.timedependent]
dimension = 2
formulation = pylith.problems.Implicit
formulation.solver = pylith.problems.SolverNonlinear

[pylithapp.timedependent.formulation.time_step]
total_time = 1.0*year
dt = 1.0*year

# ----------------------------------------------------------------------
# materials
# ----------------------------------------------------------------------
# Specify the material information for the problem.
# The material type is isotropic elastic formulated for plane strain.

[pylithapp.timedependent]
materials = [ucrust,lcrust,mantle]

[pylithapp.timedependent.materials]
ucrust = pylith.materials.ElasticPlaneStrain
lcrust = pylith.materials.ElasticPlaneStrain
mantle = pylith.materials.ElasticPlaneStrain

#[pylithapp.timedependent.materials.material]

# Upper Crust
[pylithapp.timedependent.materials.ucrust]
label = Elastic ucrust
```

```
# The id corresponds to the block number from CUBIT.
id = 1

db_properties = spatialdata.spatialdb.SimpleDB
db_properties.label = Elastic ucrust properties
db_properties.iohandler.filename = spatialdb/mat_ucrust_elastic.spatialdb
db_properties.query_type = nearest

# We are doing 2D quadrature for a triangle.
quadrature.cell = pylith.feassemble.FIATLagrange
quadrature.cell.dimension = 2

# Lower crust
[pylithapp.timedependent.materials.lcrust]
label = Elastic lower crust

# The id corresponds to the block number from CUBIT.
id = 2

db_properties = spatialdata.spatialdb.SimpleDB
db_properties.label = Elastic lcrust properties
db_properties.iohandler.filename = spatialdb/mat_lcrust_elastic.spatialdb
#db_properties.iohandler.filename = spatialdb/mat_lcrust_Maxwell.spatialdb
db_properties.query_type = nearest

# We are doing 2D quadrature for a triangle.
quadrature.cell = pylith.feassemble.FIATLagrange
quadrature.cell.dimension = 2

# Mantle
[pylithapp.timedependent.materials.mantle]
label = Elastic mantle

# The id corresponds to the block number from CUBIT.
id = 3

db_properties = spatialdata.spatialdb.SimpleDB
db_properties.label = Elastic mantle properties
db_properties.iohandler.filename = spatialdb/mat_mantle_elastic.spatialdb
#db_properties.iohandler.filename = spatialdb/mat_mantle_Maxwell.spatialdb
db_properties.query_type = nearest

# We are doing 2D quadrature for a triangle.
quadrature.cell = pylith.feassemble.FIATLagrange
quadrature.cell.dimension = 2

# ----------------------------------------------------------------------
# output
# ----------------------------------------------------------------------
# Names of output files are set in stepXX.cfg. We consolidate all of the
# output settings that are common to all of the simulations here.

[pylithapp.timedependent.formulation]
# Set the output to an array of 2 output managers.
# We will output the solution over the domain and the ground surface.
output = [domain]

# Domain
[pylithapp.problem.formulation.output.domain]
vertex_data_fields = [displacement]
writer = pylith.meshio.DataWriterHDF5

# Materials
[pylithapp.timedependent.materials.ucrust.output]
writer = pylith.meshio.DataWriterHDF5
```

```
cell_data_fields = [stress,cauchy_stress,total_strain]

# Comment this out for if rerunning Step 3 to get initial conditions for Step 8.
cell_filter = pylith.meshio.CellFilterAvg

[pylithapp.timedependent.materials.lcrust.output]
writer = pylith.meshio.DataWriterHDF5
cell_data_fields = [stress,cauchy_stress,total_strain]

# Comment this out for if rerunning Step 3 to get initial conditions for Step 8.
cell_filter = pylith.meshio.CellFilterAvg

[pylithapp.timedependent.materials.mantle.output]
writer = pylith.meshio.DataWriterHDF5
cell_data_fields = [stress,cauchy_stress,total_strain]

# Comment this out for if rerunning Step 3 to get initial conditions for Step 8.
cell_filter = pylith.meshio.CellFilterAvg

# ----------------------------------------------------------------------
# PETSc
# ----------------------------------------------------------------------
# We are using all of the default settings for PETSc except for
# specifying the block Jacobi preconditioner.  Additional PETSc
# command-line arguments may be found in the PETSc documentation.
[pylithapp.petsc]

# Preconditioner settings.
pc_type = bjacobi

# Convergence parameters.
ksp_rtol = 1.0e-50
ksp_atol = 1.0e-12

# Linear solver monitoring options.
ksp_monitor = true
ksp_converged_reason = true
ksp_error_if_not_converged = true

# Nonlinear solver monitoring options.
snes_rtol = 1.0e-50
snes_atol = 1.0e-10
snes_max_it = 100
snes_monitor = true
snes_converged_reason = true
snes_linesearch_monitor = true
snes_error_if_not_converged = true

# start_in_debugger = true
# debugger_timeout = 100

# End of file
```

```
# PyLith parameters for 3D MODELS

# The settings in this file (pylithapp.cfg) will be read automatically
# by pylith, as long as the file is placed in the run directory.

# The settings in this file will override any settings in:
# PREFIX/etc/pylithapp.cfg
# $HOME/.pyre/pylithapp/pylithapp.cfg

# The settings in this file will be overridden by any .cfg file given
# on the command line or by any command line settings.
```

```
[pylithapp]

# ----------------------------------------------------------------------
# journal
# ----------------------------------------------------------------------
# The settings below turn on journal info for the specified components.
# If you want less output to stdout, you can turn these off.
[pylithapp.journal.info]
timedependent = 1
implicit = 1
petsc = 1
solverlinear = 1
meshiocubit = 1
homogeneous = 1
elasticityimplicit = 1
fiatsimplex = 1
pylithapp = 1
materials = 1
mesh_distributor = 1

# ----------------------------------------------------------------------
# mesh_generator
# ----------------------------------------------------------------------
# The settings below control the mesh generation (importing mesh info).
# Turn on debugging output for mesh generation.
[pylithapp.mesh_generator]
debug = 1
reader = pylith.meshio.MeshIOCubit

# This component specification means we are using PyLith ASCII format,
# and we then specify the filename and number of space dimensions for
# the mesh.
[pylithapp.mesh_generator.reader]
filename = ../mesh/mesh_3d_mod6.exo

# ----------------------------------------------------------------------
# problem
# ----------------------------------------------------------------------
# Specify the problem settings.
# This is a time-dependent problem, so we select this as our problem type.
# We select a total time of 0 sec, and a time step size of 1 sec, so we
# are performing a single time step.
# The spatial dimension for this problem is 2.
# For an implicit formulation (using implicit.cfg), we will perform 1
# implicit time step from t = -1.0 to t = 0.0 (elastic solution step).
[pylithapp.timedependent]
dimension = 3
formulation = pylith.problems.Implicit
formulation.solver = pylith.problems.SolverNonlinear

[pylithapp.timedependent.formulation.time_step]
total_time = 1.0*year
dt = 1.0*year

# ----------------------------------------------------------------------
# materials
# ----------------------------------------------------------------------
# Specify the material information for the problem.
# The material type is isotropic elastic formulated for plane strain.

[pylithapp.timedependent]
materials = [ucrust,lcrust,mantle,sill,chamber]

# Upper Crust
```

```
[pylithapp.timedependent.materials.ucrust]
label = Elastic ucrust

# The id corresponds to the block number from CUBIT.
id = 1

db_properties = spatialdata.spatialdb.SimpleDB
db_properties.label = Elastic ucrust properties
db_properties.iohandler.filename = ../spatialdb/mat_ucrust_elastic.spatialdb
db_properties.query_type = nearest

# We are doing 2D quadrature for a triangle.
quadrature.cell = pylith.feassemble.FIATSimplex
quadrature.cell.dimension = 3

# Lower crust
[pylithapp.timedependent.materials.lcrust]
label = Elastic lower crust

# The id corresponds to the block number from CUBIT.
id = 2

db_properties = spatialdata.spatialdb.SimpleDB
db_properties.label = Elastic lcrust properties
db_properties.iohandler.filename = ../spatialdb/mat_lcrust_elastic.spatialdb
db_properties.query_type = nearest

# We are doing 2D quadrature for a triangle.
quadrature.cell = pylith.feassemble.FIATSimplex
quadrature.cell.dimension = 3

# Mantle
[pylithapp.timedependent.materials.mantle]
label = Elastic mantle

# The id corresponds to the block number from CUBIT.
id = 3

db_properties = spatialdata.spatialdb.SimpleDB
db_properties.label = Elastic mantle properties
db_properties.iohandler.filename = ../spatialdb/mat_mantle_elastic.spatialdb
db_properties.query_type = nearest

# We are doing 2D quadrature for a triangle.
quadrature.cell = pylith.feassemble.FIATSimplex
quadrature.cell.dimension = 3

# Sill
[pylithapp.timedependent.materials.sill]
label = Elastic sill

# The id corresponds to the block number from CUBIT.
id = 4

db_properties = spatialdata.spatialdb.SimpleDB
db_properties.label = Elastic sill properties
db_properties.iohandler.filename = ../spatialdb/mat_magmanew_elastic.spatialdb
db_properties.query_type = nearest

# We are doing 2D quadrature for a triangle.
quadrature.cell = pylith.feassemble.FIATSimplex
quadrature.cell.dimension = 3

# Chamber
[pylithapp.timedependent.materials.chamber]
```

```
label = Elastic chamber

# The id corresponds to the block number from CUBIT.
id = 5

db_properties = spatialdata.spatialdb.SimpleDB
db_properties.label = Elastic chamber properties
db_properties.iohandler.filename = ../spatialdb/mat_mush_elastic.spatialdb
db_properties.query_type = nearest

# We are doing 2D quadrature for a triangle.
quadrature.cell = pylith.feassemble.FIATSimplex
quadrature.cell.dimension = 3

# ----------------------------------------------------------------------
# output
# ----------------------------------------------------------------------
# Names of output files are set in stepXX.cfg. We consolidate all of the
# output settings that are common to all of the simulations here.

[pylithapp.timedependent.formulation]
# Set the output to an array of 2 output managers.
# We will output the solution over the domain and the ground surface.
output = [domain]

# Domain
[pylithapp.problem.formulation.output.domain]
vertex_data_fields = [displacement]
writer = pylith.meshio.DataWriterHDF5

# Materials
[pylithapp.timedependent.materials.ucrust.output]
writer = pylith.meshio.DataWriterHDF5
cell_data_fields = [stress,cauchy_stress,total_strain]

# Comment this out for if rerunning Step 3 to get initial conditions for Step 8.
cell_filter = pylith.meshio.CellFilterAvg

[pylithapp.timedependent.materials.lcrust.output]
writer = pylith.meshio.DataWriterHDF5
cell_data_fields = [stress,cauchy_stress,total_strain]

# Comment this out for if rerunning Step 3 to get initial conditions for Step 8.
cell_filter = pylith.meshio.CellFilterAvg

[pylithapp.timedependent.materials.mantle.output]
writer = pylith.meshio.DataWriterHDF5
cell_data_fields = [stress,cauchy_stress,total_strain]

# Comment this out for if rerunning Step 3 to get initial conditions for Step 8.
cell_filter = pylith.meshio.CellFilterAvg

[pylithapp.timedependent.materials.sill.output]
writer = pylith.meshio.DataWriterHDF5
cell_data_fields = [stress,cauchy_stress,total_strain]

# Comment this out for if rerunning Step 3 to get initial conditions for Step 8.
cell_filter = pylith.meshio.CellFilterAvg

[pylithapp.timedependent.materials.chamber.output]
writer = pylith.meshio.DataWriterHDF5
cell_data_fields = [stress,cauchy_stress,total_strain]

# Comment this out for if rerunning Step 3 to get initial conditions for Step 8.
cell_filter = pylith.meshio.CellFilterAvg
```

```
# ----------------------------------------------------------------------
# PETSc
# ----------------------------------------------------------------------
# We are using all of the default settings for PETSc except for
# specifying the block Jacobi preconditioner.  Additional PETSc
# command-line arguments may be found in the PETSc documentation.
[pylithapp.petsc]
malloc_dump =

# Preconditioner settings.
pc_type = asm
sub_pc_factor_shift_type = nonzero

# Convergence parameters.
ksp_rtol = 1.0e-10
ksp_atol = 1.0e-20
ksp_max_it = 1000
ksp_gmres_restart = 200

# Linear solver monitoring options.
ksp_monitor = true
ksp_converged_reason = true
ksp_error_if_not_converged = true

# Nonlinear solver monitoring options.
snes_rtol = 1.0e-10
snes_atol = 1.0e-9
snes_max_it = 100
snes_monitor = true
snes_converged_reason = true
snes_linesearch_monitor = true
snes_error_if_not_converged = true

# PETSc summary -- useful for performance information.
log_view = true

# End of file
```

SM5. Post-processing.

We subtract the gravitational stresses due to the reference model (SM1), and calculate principal stresses and pressure = (sigma1 + sigma2 + sigma3) / 3 using the python script shown below for the 3D case:

```
#!/usr/bin/env nemesis
# -*- Python -*- (syntax highlighting)
# ----------------------------------------------------------------------

import numpy
import h5py
import sys
from shutil import copyfile

from spatialdata.spatialdb.SimpleIOAscii import SimpleIOAscii
from coordsys import cs_mesh
cs = cs_mesh()

# Constants for computing reference model.
rhoUC = 2761.0
```

```
rhoLC = 2833.0
rhoM = 3300.0
vsUC = 3600.0
vsLC = 3400.0
vsM = 4500.0
vpUC = 6200.0
vpLC = 6500.0
vpM = 8100.0
g = 9.80665
z1 = -20000.0
z2 = -40000.0
stressUC = rhoUC*g*z1
stressLC = rhoLC*g*(z2 - z1)

# Compute material properties.
muUC = rhoUC*vsUC*vsUC
muLC = rhoLC*vsLC*vsLC
muM = rhoM*vsM*vsM
lamUC = rhoUC*vpUC*vpUC - 2.0*muUC
lamLC = rhoLC*vpLC*vpLC - 2.0*muLC
lamM = rhoM*vpM*vpM - 2.0*muM

def getCellCenters(vertices, cells):
    """
    Function to compute cell centers.
    """
    cellCoords = vertices[cells, :]
    cellCenters = numpy.mean(cellCoords, axis=1)
    return cellCenters

def generate(sim, fileRoot, materials):

    for material in materials:

        filenameH5 = "%s-%s.h5" % (sim, material)

        # Open HDF5 file and get coordinates, cells, and stress.
        h5 = h5py.File(filenameH5, "r")
        vertices = h5['geometry/vertices'][:]
        cells = numpy.array(h5['topology/cells'][:], dtype=numpy.int)

        filenewH5 = "%s-%s-pstresses.h5" % (sim, material)
        copyfile(filenameH5,filenewH5)
        h5new = h5py.File(filenewH5, "r+")

        # Get stresses from final time step.
        stress = h5['cell_fields/stress'][-1,:,:]
        refStress = numpy.zeros_like(stress)
        h5.close()

        # Compute coordinates of quadrature points.
        quadCoords = getCellCenters(vertices, cells)

        # Compute reference stress.
        z = quadCoords[:,2]
        coordsUC = numpy.where(z >= z1)
        coordsLC = numpy.where(numpy.logical_and(z >= z2, z < z1))
        coordsM = numpy.where(z < z2)
        if (coordsUC[0].shape[0] != 0):
            refStress[coordsUC,0] = rhoUC*g*z[coordsUC]
        if (coordsLC[0].shape[0] != 0):
            refStress[coordsLC,0] = stressUC + rhoLC*g*(z[coordsLC]-z1)
        if (coordsM[0].shape[0] != 0):
            refStress[coordsM,0] = stressUC + stressLC + rhoM*g*(z[coordsM]-z2)
        refStress[:,1] = refStress[:,0]
```

```
        refStress[:,2] = refStress[:,0]
        refStress *= -1.0
        pressureRef = (refStress[:,0] + refStress[:,1] + refStress[:,2])/3

        # Define square 3x3 array

        sigma1 = [] # principal compressive stress, negative stress in PyLith
        sigma2 = []
        sigma3 = [] # principal tensile stress, positive stress in PyLith
        theta1 = []
        theta2 = []
        theta3 = []
        pressure = []
        for cell in stress:
            stresstensor =
numpy.array([(cell[0],cell[3],cell[5]),(cell[3],cell[1],cell[4]),(cell[5],cell[4],ce
ll[2])])

        # Calculate principal stresses
            [w, v] = numpy.linalg.eigh(stresstensor)
            sigma1.append(w[0])
            sigma2.append(w[1])
            sigma3.append(w[2])
            theta1.append(v[:,0])
            theta2.append(v[:,1])
            theta3.append(v[:,2])
            pressure.append((w[0]+w[1]+w[2])/3)

        # Create pressure array as well as pressure minus reference model.
        pressure = numpy.array(pressure)
        pressureRel = pressure - pressureRef
        pressureRelneg = pressureRel*(-1)

        # change row vector to column vector
        sigma1 = numpy.array(sigma1).reshape(-1,1)
        sigma2 = numpy.array(sigma2).reshape(-1,1)
        sigma3 = numpy.array(sigma3).reshape(-1,1)

        # add zero for z column
        theta1 = numpy.array(theta1)
        theta3 = numpy.array(theta3)
        theta2 = numpy.array(theta2)

        nrows = stress.shape[0]
        ncols = stress.shape[1]

        #dataset_sigma = h5new.create_dataset('cell_fields/sigma', (1,nrows,3),
maxshape=(None,nrows,3), data=sigma)
        dataset_sigma1 = h5new.create_dataset('cell_fields/s1', (1,nrows,1),
maxshape=(None,nrows,1), data=sigma1)
        dataset_sigma2 = h5new.create_dataset('cell_fields/s2', (1,nrows,1),
maxshape=(None,nrows,1), data=sigma2)
        dataset_sigma3 = h5new.create_dataset('cell_fields/s3', (1,nrows,1),
maxshape=(None,nrows,1), data=sigma3)
        dataset_theta1 = h5new.create_dataset('cell_fields/t1', (1,nrows,3),
maxshape=(None,nrows,3), data=theta1)
        dataset_theta2 = h5new.create_dataset('cell_fields/t2', (1,nrows,3),
maxshape=(None,nrows,3), data=theta2)
        dataset_theta3 = h5new.create_dataset('cell_fields/t3', (1,nrows,3),
maxshape=(None,nrows,3), data=theta3)
        dataset_pressure = h5new.create_dataset('cell_fields/P', (1,nrows,1),
maxshape=(None,nrows,1), data=pressure)
        dataset_pressure_ref = h5new.create_dataset('cell_fields/P_ref',
(1,nrows,1), maxshape=(None,nrows,1), data=pressureRef)
```

```
        dataset_pressure_rel = h5new.create_dataset('cell_fields/P_rel',
(1,nrows,1), maxshape=(None,nrows,1), data=pressureRel)
        dataset_pressure_relneg = h5new.create_dataset('cell_fields/P_relneg',
(1,nrows,1), maxshape=(None,nrows,1), data=pressureRelneg)

        #dataset_sigma.attrs.create(name='vector_field_type',data="tensor")
        dataset_sigma1.attrs.create(name='vector_field_type',data="scalar")
        dataset_sigma2.attrs.create(name='vector_field_type',data="scalar")
        dataset_sigma3.attrs.create(name='vector_field_type',data="scalar")
        dataset_theta1.attrs.create(name='vector_field_type',data="vector")
        dataset_theta2.attrs.create(name='vector_field_type',data="vector")
        dataset_theta3.attrs.create(name='vector_field_type',data="vector")
        dataset_pressure.attrs.create(name='vector_field_type',data="scalar")
        dataset_pressure_ref.attrs.create(name='vector_field_type',data="scalar")
        dataset_pressure_rel.attrs.create(name='vector_field_type',data="scalar")
        dataset_pressure_relneg.attrs.create(name='vector_field_type',data="scalar")

        h5new.close()

    return


# ----------------------------------------------------------------------
if __name__ == "__main__":
    import argparse
    parser = argparse.ArgumentParser()
    parser.add_argument("--sim", action="store", dest="sim",
default="novel_grav_mod0")
    parser.add_argument("--file-root", action="store", dest="fileRoot",
default="mat_principal_stress")
    parser.add_argument("--materials", action="store", dest="materials",
default="ucrust,lcrust,mantle")
    args = parser.parse_args()

    materials = args.materials.split(",")
    generate(args.sim, args.fileRoot, materials)

# End of file
```